

COVER PAGE

Document downloaded by @DAEL

Sat Nov 28 21:46:01 2026
For personal use

When automatic English translation is provided, only the original document is authentic.
The EAA cannot be held responsible of any translation error

Bibliographical reference

Acoustic Tomography of the Atmosphere: Comparison of Different Reconstruction Algorithms, Gabi Fischer, Manuela Barth and Astrid Ziemann, Acta Acustica **vol. 98** (Number 4), 2012, pp. 534-545

DOI
https://doi.org/10.3813/AAA.918535

ACTA ACUSTICA UNITED WITH ACUSTICA
Vol. 98 (2012) 534 – 545
DOI 10.3813/AAA.918535

Acoustic Tomography of the Atmosphere: Comparison of Different Reconstruction Algorithms

Gabi Fischer, Manuela Barth, Astrid Ziemann*
University of Leipzig, Leipzig Institute for Meteorology, Stephanstr. 3, 04103 Leipzig, Germany.
gfischer@uni-leipzig.de

Summary
Acoustic travel-time tomography in the atmosphere is based on travel-time measurements of sound signals propagating along different known ray paths through a medium. Because the speed of sound mainly depends on temperature and flow properties, an inversion of these travel times allows an estimation of temperature and wind velocity fields. The main reconstruction techniques for solving such inverse problems are least-squares methods and stochastic inversion algorithms. In this study, five representatives belonging to these types of inverse approaches are evaluated by reconstructions of two-dimensional temperature distributions from synthetically generated and experimental data. The comparison of the reconstruction results reveals several differences between the algorithms concerning spatial resolution of the reconstructed image, accuracy, and computational efficiency. The stochastic approach provides accurate reconstructions of spatially highly resolved temperature fields when the turbulence characteristic is chosen carefully. Nevertheless, the choice of suitable turbulence parameters, the determination of measurement errors prior to an experiment as well as comparatively high memory requirements of this method are unfavorable for real-time analysis of measured data although possible. In contrast, fast and simple on-site interpretations of temperature fields with acceptable accuracy are feasible with least-squares methods.

PACS no. 43.20.Dk, 43.28.Vd, 43.28.We

1. Introduction

Tomography is an imaging technique which produces cross-sectional images of an object or medium without disturbances due to an insertion of sensors. The basic principle of tomographic techniques is the analysis of waves which propagate along different paths through a medium and are measurably altered by the fluid properties along the propagation paths. Subsequently, an inversion of such measurements can be used to estimate the spatial distribution of the influencing parameters within the measurement area or volume. The application of actively generated mechanical or electromagnetic waves require the usage of a certain amount of devices. If the setup consists of S sources and R receivers (total number of sensors: $S + R$) up to $(S \cdot R)$ measurements across the medium under study can be obtained, in contrast to conventional point sensors, where only one measurement per sensor is obtained. Because of this comparatively high number of data sets per sensor as well as the remote sensing aspect, the tomographic technique is a very helpful and efficient tool for many problems in science of which just a few are mentioned here. In medicine computer tomography, positron emission tomography, magnetic resonance imaging, and ultrasound tomography are used to visualize the interior of human or animal bodies. Furthermore, seismic tomography offers the possibility to investigate the properties of the Earth's interior [1] whereas with ocean acoustic tomography the distribution and trend of temperatures and currents in the ocean are determined [2]. The principle of tomography was also transferred to the atmosphere, e.g. acoustic travel-time tomography of the atmosphere for visualization of temperature and wind velocity fields [3, 4, 5], ionospheric tomography for imaging of the structure of ionospheric irregularities [6], tomographic DOAS (Differential Optical Absorption Spectroscopy) for visualization of concentration fields of air pollutants or other trace gases [7, 8], and GNSS water vapor tomography for computing spatially resolved humidity fields [9].

All tomographic methods use projections of an object or medium from many different angles of view to reconstruct two-dimensional or three-dimensional fields of unknown physical parameters. The inversion of the measured data requires reliable and efficient numerical algorithms. For real-time analyses, which are necessary to monitor the

Received 10 June 2011,
accepted 10 May 2012.

* Current affiliation: TU Dresden, Institute of Hydrology and Meteorology, Chair of Meteorology

© S. Hirzel Verlag · EAA

desired quantities, fast and robust inversion techniques are demanded. However, it is not immediately clear which algorithm is suitable to provide an accurate as well as fast and stable solution of the given inversion problem. For this reason, the comparison of different inversion techniques concerning their spatial resolution of the tomographic image, reconstruction accuracy, numerical stability, and computational efficiency is essential to decide which algorithm is appropriate for a certain application.

In this study different inversion algorithms are compared which are applied to meteorological problems performing acoustic travel-time tomography in the atmosphere. This method uses the dependency of the speed of sound on atmospheric conditions to estimate spatially resolved temperature and wind velocity fields. The inversion problem is the reconstruction of the unknown meteorological quantities from the measured travel-time data along different sound propagation paths between known locations of several sources and receivers. Since Radon's first tomographic approach in 1917 [10] many different inversion methods have been developed. The main inversion techniques in acoustic travel-time tomography of the atmosphere are stochastic and least-squares methods whose development and progress in the last years are described in [11].

The stochastic inversion (SI) was applied by Spiesberger and Fristrup [12] as well as Wilson and Thomson [3] in theoretical and experimental studies of the atmosphere for the first time. This numerical algorithm enables one to reconstruct the unknown temperatures and wind vectors at given points within the investigation area. In acoustic travel-time tomography, stochastic inversion most often is applied to reconstruct small-scale turbulent distributions of these meteorological fields in the atmospheric boundary layer [3, 5, 13, 14]. This ability is a main advantage of SI compared to the other analyzed algorithms that are included in this study. The resulting tomographic images are composed of a mean value of the scanned area and spatial fluctuations at given points within the tomographic area. The conventional stochastic inversion was improved by Vecherin *et al.* [14, 5] by realizing a time-dependent stochastic inversion. This method provides an increased number of travel-time data without increasing the number of sources and receivers and yields reconstruction results which were quite better than the results obtained by conventional stochastic inversion.

Like the stochastic approach, applications of least-squares methods demand a discretization of the inversion problem. In this study the investigation area is discretized into cells with defined sizes. It is assumed that the temperature value in one grid cell is constant and represents an area or volume average. The first implementation of such an approach in the atmosphere was done by Ziemann *et al.* [15] using an iterative algebraic reconstruction technique that was further applied in different atmospheric studies (e.g., [4, 16, 17]). Here, four different least-squares methods were investigated. Three of them belong to the class of iterative inversion algorithms, whereas the other one is a matrix inversion method [18].

The focus of the present study is on reconstructions of scalar temperature fields. It has to be noticed that the results of this comparative study are not only limited to this special situation but are also transferable to similar tomographic applications. In contrast, reconstructions of vector fields (e.g. wind velocity fields in case of acoustic travel-time tomography [17]) with different inversion algorithms require separate analyses which will be the focus of subsequent studies.

For a general comparison of the five types of inversion techniques, the same initial data basis was used. Furthermore, no time dependency within the data was allowed, thus applying the conventional stochastic approach instead of time-dependent stochastic inversion. In the following section, detailed descriptions of the analyzed inversion algorithms are presented. To characterize the different inversion algorithms, numerical as well as experimental sensitivity tests with respect to spatial resolution and accuracy (deviation between reconstruction and original distribution) of the tomographic image as well as computational effort were performed and described in section 3 and 4, respectively. Section 5 contains concluding remarks and an outlook to further investigations.

2. Tomographic inversion algorithms

Remote sensing by acoustic travel-time tomography enables the determination of temperature distributions without influencing the investigation area or volume by insertion of sensors. Therefore, several sound sources and receivers have to be arranged around the area of investigation such that the resulting sound ray paths cover the area as uniformly as possible. Hence, travel times of sound signals along different ray paths can be recorded which are influenced by the temperature and wind vector distribution within the traversed tomographic area. In a moving atmosphere, assuming that the square of the wind speed v^2 is much smaller than the square of the Laplacian (adiabatic) sound speed c_L^2 ($v^2 \ll c_\mathrm{L}^2$), the group velocity of a sound impulse can be reduced to the so called effective sound speed along the i-th ray path [19]

$$c_\mathrm{eff}(\mathbf{r}) = c_\mathrm{L}(\mathbf{r}) + \mathbf{e}_i \cdot \mathbf{v}(\mathbf{r}), \tag{1}$$

with the position vector $\mathbf{r} = (x, y, z)$ and the unit vector $\mathbf{e}_i$ in direction of the i-th sound propagation path. The Laplacian sound speed depicts the temperature dependency of an adiabatic sound propagation in a motionless atmosphere,

$$c_\mathrm{L}(\mathbf{r}) = \sqrt{\gamma_\mathrm{d} R_\mathrm{d} T_\mathrm{av}(\mathbf{r})}. \tag{2}$$

The quantities γ_d and R_d denote the ratio of specific heat capacities at constant pressure and constant volume and the specific gas constant for dry air (index d), respectively. In contrast to the thermodynamic temperature T, the acoustic virtual temperature $T_\mathrm{av} = T(1+0.513q)$ considers

the humidity of air, where q is the specific humidity in kg water vapor per kg humid air [20]. For simplification, the acoustic virtual temperature, which was tomographically reconstructed in this study, is referred to as temperature in the following. Furthermore, although all tomographic algorithms used in this study can be applied for reconstructions of three-dimensional temperature distributions, present analyses concentrate on two-dimensional temperature fields.

Temperature reconstructions in a moving atmosphere using least-squares methods require a pre-separation of wind vector and temperature influence on the measured travel times, whereas for a stochastic inversion this step is not necessary. However, only temperature dependent travel-time data are used here to compare the reconstruction results of the different inversion algorithms based on the same initial data. Such travel times are determined after separation of the wind and temperature influence on the effective sound speed using bidirectional or reciprocal sound ray paths [16, 21]. Although the separation involves uncertainties on the reconstructed fields [16], these uncertainties result independently of the used reconstruction algorithm. After removing the wind influence or in a motionless medium (which is the case for all presented analyses in this study), the temperature dependent travel time τ_i along the i-th sound ray results from the path integral over the reciprocal Laplacian sound speed along the propagation path L_i between a sound source and a receiver

$$\tau_i = \int_{L_i} \frac{\mathrm{d}l}{c_\mathrm{L}(\mathbf{r}_h)}, \tag{3}$$

where $\mathrm{d}l$ is a length element along L_i with $i = 1, \ldots, I$. I denotes the total number of propagation paths, normally given by the number of sources and receivers ($I = S \cdot R$), $\mathbf{r}_h = (x, y)$ is the horizontal position vector. Considering equation (3) the inverse problem is to estimate spatially distributed values of the Laplacian sound speed using a suitable numerical algorithm and subsequently calculate temperature values according to equation (2). In the case of ill-posed problems (insufficient number of sound rays and/or noisy data) *a priori* information is needed to solve equation (3). There are different approaches to consider this information. On the one hand the *a priori* information can be implicitly included by the algorithm. On the other hand it can be explicitly included by the choice of algorithm specific parameters. Investigations about the impact of the above mentioned options on the reconstruction accuracy of all algorithms were conducted and included into the present study.

2.1. Least-squares methods

Equation (3) can be solved inversely using least-squares methods which minimize the sum of quadratic differences between the reconstructed and the measured travel times. For this purpose, equation (3) has to be discretized. In this study, the tomographic domain is subdivided into rectangular grid cells with finite sizes. Inside each cell the reconstructed temperature values are assumed to be constant which is an *a priori* assumption for this approach. If the total number of travel times along different propagation paths I is greater than the number of grid cells J the problem is overdetermined, if both are equal the problem is just-determined, otherwise the problem is underdetermined ($I < J$) [2]. Except for the just-determined case, equation system (3) has no unique solution. The solution of an underdetermined problem is determined by the *a priori* information (first guess of the searched distribution). For this reason, only overdetermined problems were considered in the following. Note that this condition limited the discretization of the tomographic field using least-squares approach such that the number and size of the grid cells could not be chosen arbitrarily for a given number of sound ray paths.

The resulting basic equation after discretization of equation (3) is

$$\boldsymbol{\tau} = \mathbf{L}\mathbf{s}, \tag{4}$$

where $\boldsymbol{\tau}$ is the travel-time vector containing I travel-time elements, $\mathbf{L}$ is the $(I \times J)$ sound ray segment matrix and $\mathbf{s}$ is the slowness vector containing J elements of reciprocal Laplacian sound speed within each grid cell. A direct least-squares method to solve equation (4) is a matrix inversion (MI) algorithm which estimates a direct inversion of $\mathbf{L}$. To find a solution for the unknown slowness vector, equation (4) has to be multiplied by the generalized inverse of the sound ray segment matrix $\mathbf{L}^{-1}$ resulting in $\mathbf{s} = \mathbf{L}^{-1}\boldsymbol{\tau}$. In the present study, the generalized inverse is estimated using a singular value decomposition scheme described in [22].

An indirect solution of the system of equations (4) is found with iterative reconstruction techniques (IRTs). In contrast to MI, IRTs are applicable to huge and sparse systems of equations and are further characterized by their simple applicability. There are numerous IRTs which originate from Kaczmarz's method [23]. All IRTs have in common that in contrast to MI, the searched slowness distribution is estimated iteratively. For this reason, equation (4) is written in component notation

$$\tau_i = \sum_{j=1}^{J} l_{ij} s_j, \tag{5}$$

where l_{ij} is the path length of the i-th sound ray within the j-th grid cell. Starting point of the iteration process is an initial distribution of reciprocal Laplacian sound speed values s_j (slowness within j-th cell), which could be achieved by a back projection of given travel times τ_i onto the J grid cells. In the first iterative step, this currently estimated slowness distribution is used to calculate travel times for all sound ray paths according to the spatial arrangement of sources and receivers. Then, differences between calculated and given travel times are calculated to derive corrections for the previously estimated slowness field (forward modeling). Now, the corrected slowness values serve as basis for the calculation of travel times and so on. This iterative process continues until reaching

convergence or an abort criterion. In the case of an overdetermined problem, the slowness vector follows a constant trajectory around the true value of the slowness vector after a high number of iterations (cyclic convergence).

In principle, the IRTs converge to the minimum norm of the minimal deviation of a pseudo solution. Thereby, the most likely solution may not be consistent with the true solution [24]. Please note that after a sufficient high number of iterations, the results reconstructed by an IRT algorithm converge to the solution of MI. However, in this study the iteration process was stopped after reaching a semi-convergence to regularize the system of equations according to Natterer [25]. Here, semi-convergence means that a satisfactory solution is obtained after a certain number of iteration steps after which the reconstruction result get worse and artifacts may occur. This termination criterion can be determined in numerical studies. In this study, the reconstruction results using IRTs are obtained after a comparatively small number of iterations. Because of that, the results of IRTs do not match those of MI exactly.

Three different iterative methods are considered, which differ from each other in the way how the corrections are calculated and applied to the previous slowness values. First, an algebraic reconstruction technique (ART) was chosen which was formerly developed for medical applications using computer tomography [26, 27]. The iterative process is built-up such that during one iteration step n all I sound ray paths are considered one after another to calculate actual improved slownesses. During each sub-step (numbering $k = 1 \dots I$) slowness corrections are calculated and added to the previous slowness values s_j^k in these grid cells which are passed by the particular sound ray. In the end, the actual improved slowness s_j^{k+1} in the j-th cell of iteration sub-step k can be written as

$$s_j^{k+1} = s_j^k + l_{ij} \frac{\tau_i - \tau_i^k}{\sum_{j=1}^{J} l_{ij}^2}. \tag{6}$$

The measured (given) and estimated travel times (using equation (5)) along sound ray i in iteration sub-step k are denoted as τ_i and τ_i^k, respectively.

For acoustic travel-time tomography of the atmosphere, an upgrade of this algorithm was applied by Ziemann *et al.* [15] first. This algorithm is referred to as simultaneous iterative reconstruction technique (SIRT) and is characterized as a method with satisfactory convergence and stability properties as well as simple handling, especially during real-time evaluation. During one iteration step n, the used SIRT algorithm calculates weighted slowness corrections considering all given travel-time data at a first step. These values are added to the previous slownesses of each grid cell to estimate the actual improved slownesses s_j^{n+1} [17]:

$$s_j^{n+1} = s_j^n + \frac{1}{W_j} \sum_{i=1}^{I} l_{ij} \frac{\tau_i - \tau_i^n}{\sum_{j=1}^{J} l_{ij}}, \tag{7}$$

where $W_j = \sum_{i=1}^{I} l_{ij}$ is the total sum of sound ray segments in grid cell j. As for ART, τ_i are measured travel times and τ_i^n are estimated travel times for the slowness values s_j^n according to equation (5).

The third studied algorithm is a multiplicative algebraic reconstruction technique (MART). This algorithm was already analyzed in [6] for applications to ionospheric tomography and is characterized by a multiplicative correction,

$$s_j^{k+1} = s_j^k \cdot \left(\frac{\tau_i}{\tau_i^k} \right)^{\frac{l_{ij}}{\sqrt{\sum_{j=1}^{J} l_{ij}^2}}}. \tag{8}$$

Similar to ART, equation (8) has to be repeated k times to complete one iteration step n. Furthermore, according to equations (6) and (8) the results of the reconstruction algorithms ART as well as MART depend on the order of the considered sound rays in the iterative process.

2.2. Stochastic inversion algorithm

In contrast to least-squares methods, stochastic inversion (SI) algorithms minimize the expected squared deviation of the reconstructed field from the original slowness distribution. Furthermore, the unknown temperature distributions are calculated at defined spatial points in the investigation area. An advantage of SI is that the accuracy of the tomographic images is independent of the number of chosen reconstruction points. Thus, it is not necessary to reconstruct highly resolved temperature fields to reflect the continuous distribution that are found in the atmosphere (this can be achieved with interpolation of a coarse spatial resolution as well), but it is essential to visualize small-scale turbulent temperature structures.

Characteristic of SI is that temperature distributions are calculated in two steps. Firstly, a mean temperature value for the whole investigation area is estimated while secondly spatial temperature fluctuations at given points within the area are determined using a suitable turbulence model. The total temperature field that was analyzed in the present study is obtained by adding the temperature fluctuations to the mean value. Please note that for the least-squares methods, the total field is immediately estimated since the approach of decomposition is not necessary for the realization of the inversion in this case.

Starting point of SI calculations is the Reynolds decomposition [28] of the Laplacian sound speed and the temperature in a spatially average (overbar) and a fluctuating part (tilde),

$$c_{\mathrm{L}}(\mathbf{r}_h) = \overline{c}_{\mathrm{L}} + \widetilde{c}_{\mathrm{L}}(\mathbf{r}_h), \tag{9}$$

$$T_{\mathrm{av}}(\mathbf{r}_h) = \overline{T}_{\mathrm{av}} + \widetilde{T}_{\mathrm{av}}(\mathbf{r}_h). \tag{10}$$

As described in [14], in a real atmosphere the absolute values of the Laplacian sound speed fluctuations are much smaller than the spatial average. Thus, equation (3) can be linearized to the first order of these fluctuations (neglecting higher order terms in Taylor expansion). Furthermore, straight line propagation can be approximated which yields the following linearized equation for SI,

$$\tau_i = \frac{L_i}{\overline{c}_{\mathrm{L}}} - \frac{1}{\overline{c}_{\mathrm{L}}^2} \int_{L_i} \frac{\overline{c}_{\mathrm{L}}}{2\overline{T}_{\mathrm{av}}} \widetilde{T}_{\mathrm{av}}(\mathbf{r}_h) \mathrm{d}l \tag{11}$$

with the total length of the i-th sound ray path $L_i = \sum_{j=1}^{J} l_{ij}$. After setting the fluctuating part to zero an averaged temperature value for the whole tomographic area is determined using the least-squares estimation,

$$\overline{T}_{\mathrm{av}} = \frac{\overline{c}_{\mathrm{L}}^2}{\gamma_d R_{\mathbf{d}}} \text{ with } \overline{c}_{\mathrm{L}} = \frac{1}{I} \sum_{i=1}^{I} \frac{L_i}{\tau_i}. \tag{12}$$

Subsequently, the temperature fluctuation $\tilde{T}_{\mathrm{av}}(\mathbf{r}_h)$ has to be reconstructed at given points within the area of investigation. Compared to the other algorithms, SI requires *a priori* information about the scanned medium as well. Using the SI approach, it is assumed that the fluctuations are randomly distributed with a known spatial covariance function of temperature $B_T(\mathbf{r}_h)$, which explicitly has to be selected [3, 29]. The different forms of this function used in literature contain two turbulence parameters, correlation length l_T and variance of temperature fluctuations σ_T^2, which also have to be known. The variance of temperature can be derived by additional conventional measurements or from turbulence theories [3]. Substantially, SI is very sensitive to l_T. According to [11], l_T is an adjustable parameter in SI which has to be chosen carefully such that the reconstruction errors are as small as possible and the value of l_T has nearly the size of the smallest reconstructed turbulent eddies in the investigation area. It has to be noticed that the reconstruction results become sufficiently accurate, when the used correlation length is similar or larger than the actual correlation length [13]. In contrast, given an accurate correlation length, the reconstructed distributions of temperature are not essentially dependent on the form of the covariance function (Karman, Gaussian, exponential) which is described in [13]. Natural conditions in the atmosphere are well reflected using a Gaussian covariance function $B_T^G(\mathbf{r}_h)$ [11]. Furthermore, in many practical tomographic applications (e.g. [3, 5]), $B_T^G(\mathbf{r}_h)$ is used because of its option to determine the searched covariance matrices partly analytically, which reduces the numerical errors and efforts.

These turbulence characteristics together with $\overline{T}_{\mathrm{av}}$ are used to calculate the so called model-data covariance matrix $\mathbf{R_{md}}$ and the data-data covariance matrix $\mathbf{R_{dd}}$ to determine a solution for equation (11),

$$\mathbf{m} = \mathbf{R_{md}} \mathbf{R_{dd}^{-1}} \mathbf{d}. \tag{13}$$

Thereby, the model vector $\mathbf{m}$ contains estimates of J elements of $\tilde{T}_{\mathrm{av}}$ which must be reconstructed, whereas the data vector $\mathbf{d}$ contains I elements of $d_i = \overline{c}_{\mathrm{L}} L_i - \overline{c}_{\mathrm{L}}^2 \tau_i$. A detailed description of the mathematical formulas for $\mathbf{R_{md}}$ and $\mathbf{R_{dd}}$ can be found in [3, 14]. In this study, the Gaussian covariance function was used by calculating $\mathbf{R_{dd}}$ partly and $\mathbf{R_{md}}$ fully analytically, respectively.

3. Sensitivity studies with synthetic data

First, the properties of all above presented inversion algorithms were analyzed under ideal conditions with given synthetically generated travel-time data from simulated temperature distributions. The advantage of such numerical studies is that optimal reconstruction parameters for the individual algorithms can be estimated before starting applications under natural experimental conditions. Moreover, the results of this numerical study enable one to choose the optimal inversion algorithm for a given tomographic problem during the preparation of experimental studies.

For numerical sensitivity studies test setups with 8 sound sources and 8 receivers as well as 16 sources and 16 receivers were chosen, which are arranged in a square field with 2.0 m base length. In an experimental application in the real atmosphere both temperature and wind vector affect the sound propagation between the acoustic devices. In order to obtain only temperature dependent travel times the sources and receivers were arranged pairwise with a horizontal distance of 20 cm such that both meteorological influences can be separated using bidirectional sound ray paths [16, 21]. Applying an optimization procedure according to [30], the acoustic devices were located around the test area such that the sound rays between the sources and receivers crossed the investigation area homogeneously. The resulting arrangement for the 8 source-receiver pairs and the corresponding 56 sound ray paths is illustrated in Figure 1. Please note that the ray paths between the sources and receivers of the individual source-receiver pairs with a length of 20 cm were neglected in the analyses.

After defining the test setups, 500 randomly simulated temperature fields are generated. All simulations contain a homogeneous background temperature of $T_{\mathrm{av},0} = 15$ °C, which is superposed by locally warmer inhomogeneities of different intensity. The temperature distributions including a so called Gaussian inhomogeneity are calculated according to

$$T_{\mathrm{av}}(x, y) = T_{\mathrm{av},0} + \delta \cdot \exp\left\{ -\left(\frac{(x - x_0)^2}{2\sigma_x^2} + \frac{(y - y_0)^2}{2\sigma_y^2} \right) \right\}. \tag{14}$$

The amplification factor of temperature change δ (only positive sign) was randomly varied between zero and a maximum value of 3 K. The extent of the inhomogeneity in x- and y-direction is marked as σ_x and σ_y, respectively. Both values were varied independently between 0.1 m and 0.5 m. The coordinate (x_0,y_0) denotes the location of the temperature extremum which was randomly determined within the tomographic area: ([0−2.0 m], [0−2.0 m]). The so generated 500 random temperature distributions in addition to the well-known positions of the acoustic devices were used to calculate the corresponding synthetic travel-time data. These travel-time data served as initial data for the numerical sensitivity study using different inversion algorithms.

For least-squares methods, in particular the MI method, the highest possible spatial resolution of the investigation

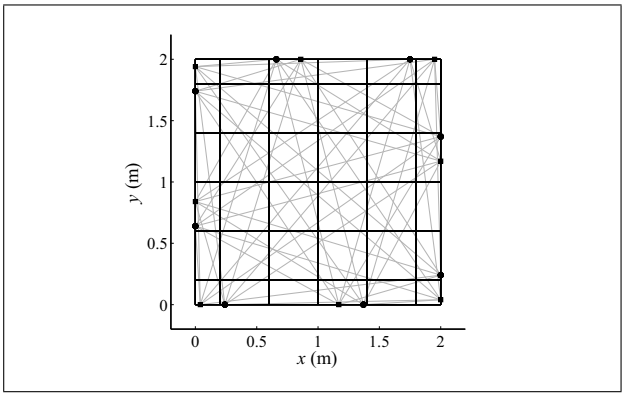


Figure 1. Setup of the tomographic array used for sensitivity studies with 8 sources (squares) and 8 receivers (circles). For tomographic reconstructions applying least-squares methods, the domain is subdivided into (0.4 × 0.4) m^2 grid cells (black lines) which are crossed by 56 different sound ray paths (gray lines).

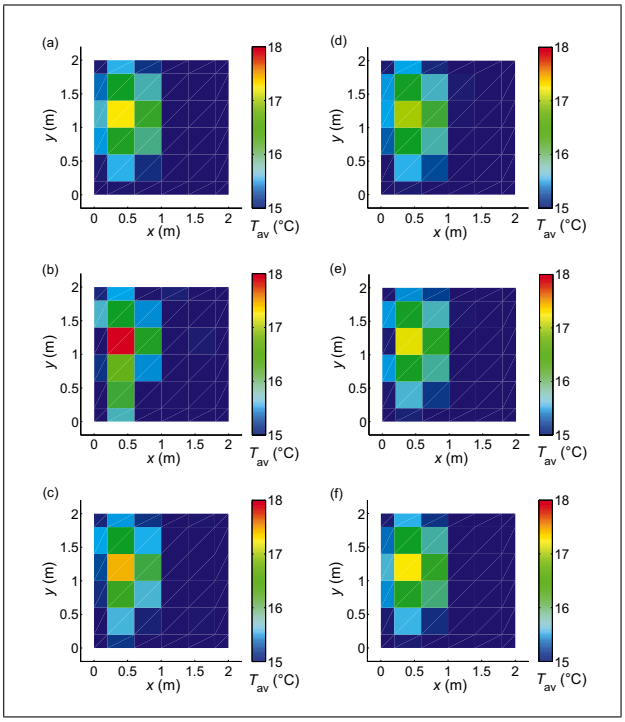


Figure 2. Simulated (a) and reconstructed acoustic virtual temperature field using MI (b), ART (c), MART (d), SIRT (e) and SI (f) for the tomographic array given in Figure 1.

area has to be identified. Therefore, the condition number α, which characterizes the ratio between the maximum and the minimum singular value of the sound ray segment matrix $\mathbf{L}$, has been calculated [31]. If α is close to one, $\mathbf{L}$ will be well-conditioned whereas large values of α indicate an ill-conditioned $\mathbf{L}$. Thus, the closer the value of α to one the more accurate is the inverse of $\mathbf{L}$ which increases the accuracy of the reconstructed temperature values as well. Using grid cells with an edge length of 0.4 m for 8 source-receiver pairs arranged around the field, the condition number yields $\alpha = 11.4$. This is still an acceptable value to achieve proper reconstruction results. To determine accurate temperature fields using the other least-squares methods, the same spatial resolution of the tomographic image with a grid size of (0.4 × 0.4) m^2 was chosen for this setup. Note that a duplication of the number of devices enables one to achieve acceptable reconstruction results with a grid cell size of (0.25 × 0.25) m^2 ($\alpha = 14.2$) yielding tomographic images with a higher spatial resolution.

To estimate the quality of the inversion algorithms, the reconstructed temperature fields were compared with the simulated ones. The performance of this quality analysis is not immediately clear because of the different discretization of equation 3 using least-squares methods and the stochastic method. A direct comparison of temperature values at the grid points of highly resolved fields between the reconstructed and simulated field is only possible for SI. In contrast, temperature fields reconstructed with least-squares methods have a coarser spatial resolution and the temperature value within one grid cell represents an average value for this subsection of the investigation area. Since the least-squares methods are not able to reconstruct small-scale turbulent temperature structures the considerations of accuracy are performed here for the coarser spatial resolution. Therefore, the 500 simulated distributions were created with a high spatial resolution in a first step. Then, these distributions are averaged with respect to the spatial resolution of least-squares methods (calculating the arithmetic average of all temperatures located within one grid cell) to estimate the quality of the reconstructed temperature value within each grid cell. The same averaging procedure was repeated for SI after reconstructing the temperature values with a high resolution of 1 cm (distance between two adjacent points). It is worthwhile to notice that if spatially averaged temperature values (calculated according to grid cell sizes of least-squares methods) of SI agree well with simulations, highly resolved temperature values at the grid points will be reconstructed with an acceptable accuracy as well.

Figure 2 shows an example of one simulated temperature distribution as well as the reconstructed tomograms using ART, MART, SIRT, MI and SI. The simulated temperature distribution has a hot spot near the left border of the test field. This inhomogeneity is characterized by a maximum temperature change of $\delta = 2.82$ K and characteristic lengths of $\sigma_x = 0.23$ m and $\sigma_y = 0.44$ m. The synthetic temperature distribution was generated with a spatial resolution of (0.01 × 0.01) m^2. For the comparison of the reconstruction results of least-squares methods with the simulated field, the highly resolved simulated temperature field was averaged to a resolution of (0.4 × 0.4) m^2.

In principle, prior to real experiments test calculations with the intended source-receiver setup and simulated temperature distributions can be used to determine a convergence criterion or a fixed number of iterations where semi-convergence is reached for IRTs (see section 2.1). Here, a fixed number of iterations was determined after which the reconstruction results do not become better but rather

worse considering the difference between the simulated and the reconstructed temperature field after each iteration step. Semi-convergence for ART and MART was achieved after 10 iteration steps whereas SIRT yielded best results after 50 iterations. As the temperature distribution in a natural atmosphere is continuous, after each iteration step a slight averaging between the grid cell itself and adjacent grid cells was implemented (see equation (12) in [21]) in order to almost realistically reconstruct the continuous temperature distribution. Therefore, a weighting factor w has been introduced as a measure of the strength of linkage between the slowness values of the neighboring grid cells. Analyses of all 500 synthetic travel-time data sets yielded the best results with weak linkages of adjacent grid cells of $w = 0.001$ for ART and MART as well as $w = 0.01$ for SIRT. The latter agrees with the results described in [32].

Tomographic images achieved with SI were calculated as described in section 2.2 using a constant correlation length of 1.0 m for all reconstructions which corresponds to the size of the maximum inhomogeneity in the field in accordance with the definition of σ_x and σ_y. For each individual reconstruction the variance of temperature fluctuations was determined from the original simulation. In the presented example in Figure 2a σ_T^2 is 0.44 K^2.

The comparison of the reconstructions and the given simulation in Figure 2 generally shows that all inversion techniques are able to determine the structure of the temperature inhomogeneity at the correct location. Largest temperature differences occur in the heated area and at the borders of the tomographic area due to the lower number of sound rays in the smaller boundary cells. Obviously, the temperature field reconstructed by MI produces the largest differences compared to the simulation whereas the magnitude of the inhomogeneity is overestimated. To quantitatively determine the differences between the reconstruction results of the different algorithms, the root mean square error (RMSE) between the simulated $T^j_{\mathrm{av,simu}}$ (original distribution) and the reconstructed temperature distribution $T^j_{\mathrm{av,reco}}$ was calculated as

$$\mathrm{RMSE} = \sqrt{\frac{\sum_{j=1}^{J}\left(T^j_{\mathrm{av,simu}} - T^j_{\mathrm{av,reco}}\right)^2}{J}}. \qquad (15)$$

For the example in Figure 2, the RMSE value of the reconstruction using MI was 0.3 K. ART, SIRT, and MART yielded reconstruction results with an RMSE of 0.12 K, 0.11 K, and 0.07 K, respectively.

The results achieved by SI are nearly identical with the original temperature field. For this algorithm the calculated RMSE value is 0.02 K which is one order of magnitude smaller than the RMSE value of MI.

Table I shows mean RMSE values and corresponding standard deviations (STDs) for 8 source-receiver pairs (see Figure 1) and 16 source-receiver pairs. Each mean RMSE is taken from individual RMSE values which have been calculated for all 500 randomly generated temperature fields and the corresponding reconstructed distributions using the analyzed inversion algorithms. Considering the mean RMSE results of least-squares methods for 8 source-receiver pairs, the IRTs yield smaller values compared to MI. The mean RMSE value for SI is in turn smaller than the values of all least-squares methods. However, STD of SI exceeds STD of SIRT and MART which indicates a greater spread of single RMSE values of SI compared to SIRT and MART. This greater spread for SI results from artifacts in the tomograms. Such artifacts occur especially in areas that are not affected by the temperature inhomogeneity, while the inhomogeneities are well reconstructed. Thus, the optimal choice of an algorithm for the underlying arrangement with 8 source-receiver pairs depends on the specific application and problem. If stable results throughout the whole area are demanded, the least-squares methods MART and SIRT are preferable. An improvement of SI results using the same number of sensors could be achieved by considering the reconstruction results at previous times (time-dependent SI, [5, 14]).

Table I. Mean RMSE values ($\overline{RMSE}$) and standard deviations (STD) for two different test setups (different number of source-receiver (S-R) pairs) each taken from individual RMSE values which have been calculated for all 500 randomly generated temperature fields and the corresponding reconstructed distributions using the indicated inversion algorithms. All values in Kelvin

Algorithm	8 S-R-pairs		16 S-R-pairs	
	$\overline{RMSE}$	STD	$\overline{RMSE}$	STD
MI	0.11	0.076	0.05	0.032
ART	0.06	0.043	0.07	0.047
MART	0.06	0.040	0.06	0.040
SIRT	0.05	0.036	0.03	0.022
SI	0.03	0.041	0.01	0.007

An increase of given travel-time data due to a doubling of the number of source-receiver pairs produces on average quite better reconstruction results for MI, SIRT, and SI. In this case, mean RMSE and STD of SI is much smaller than the values of all least-squares methods. This improvement of the reconstruction output for SI results from the fact that with increasing number of sensors the conditioning of the $\mathbf{R_{dd}}$ matrix increases as well, which leads to a reduction of mean RMSE and STD. Because of this high accuracy, SI is in favor of reconstructing small-scale structures within a medium using 16 source-receiver pairs.

Under field conditions, temperature differences of several Kelvin could occur horizontally as well as vertically in the atmospheric boundary layer, e.g. in air layers over inhomogeneous terrain or during warm and sunny days in street canyons [33]. Knowing the quality of the inversion algorithms during conditions with a high temperature inhomogeneity enables one to choose a suitable algorithm for visualizing such structures. Therefore, in this study the dependence of the accuracy of the reconstruction results on the strength of temperature inhomogeneity within the tomographic array was also analyzed. In Figure 3 the RMSE value for each reconstruction using the test setup with 8 as well as 16 source-receiver pairs is plotted against

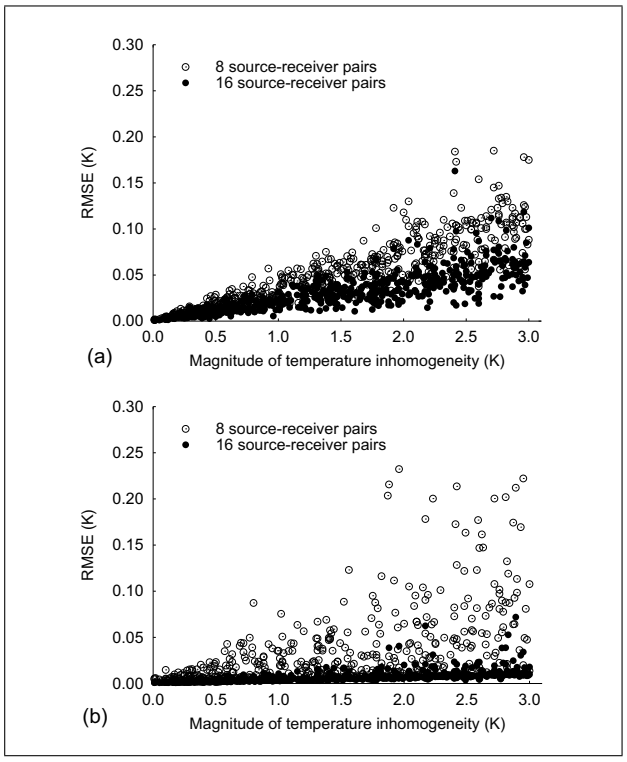


Figure 3. Correlation between magnitude of temperature inhomogeneity δ of the simulated distribution and accuracy of the tomographic reconstruction (RMSE) for SIRT (a) and SI (b).

the maximum temperature change δ of the corresponding simulation. Representative for the least-squares methods, RMSE results of SIRT are displayed in Figure 3a because this algorithm yielded the best reconstruction results of all investigated least-squares methods. Obviously, increasing temperature differences within the array produce increasing RMSE values which in turn involves a decrease in absolute reconstruction accuracy. In contrast, this constant slope achieved by all least-squares methods is not clearly visible in the analyses of SI results (see Figure 3b). In most cases, the calculated RMSE values using SI are less than 0.1 K. However, with increasing temperature difference the spreading of the RMSE values increases, too. Particularly with regard to the test setup with 8 source-receiver pairs, the results of SI may become worse in situations with high small scale temperature inhomogeneities in the analyzed area. In some situations SIRT achieved even more accurate reconstructions than SI.

In these cases artifacts are visible in the temperature tomograms reconstructed by SI due to an ill-conditioned $\mathbf{R_{dd}}$ matrix. With increasing local temperature inhomogeneity the strength of the artifacts increases as well. According to [14], a regularization of $\mathbf{R_{dd}}$ is possible considering noise in the data. Noise can be included by adding an additional term to the main diagonal of the $\mathbf{R_{dd}}$ matrix. Thus, the condition of the matrix can be improved [14]. A disadvantage of this regularization is that the reconstructed temperature distributions are also smoothed. Sensitivity analyses showed that the strength of the smoothing increases with an increase of noise such that this regularization should be applied carefully.

Furthermore, it should be noticed that according to Table I a doubling of the number of acoustic devices reduces the RMSE values of SIRT and SI significantly. Figure 3 illustrates that the higher number of acoustic devices and therewith the higher amount of travel-time data significantly improves the quality of the reconstruction results, especially of SI. In contrast, with a number of source-receiver pairs lower than 8, the SI method is also applicable, but a careful regularization of the $\mathbf{R_{dd}}$ matrix and choice of turbulence parameters is required.

Another aspect when comparing the inversion algorithms is their applicability to provide the searched quantities in suitable time with low computational effort. In particular, this plays an important role for real-time data evaluation during measurement campaigns. Moreover, fast real-time analyses can be used to control processes operationally, e.g., to control the temperature in an area or volume of interest where a certain value should not be exceeded. With recent advances in computer technology, the computational effort is not a limiting factor anymore, especially for memory consuming algorithms like MI and SI. Still lower requirements concerning storage capacity provide IRTs. By contrast, the SI algorithm needs an increased storage capacity and comparatively high computational time for calculating the data-data and model-data matrices. However, knowing the positions of acoustic devices, the turbulence characteristics and the measurement errors before starting a real measurement, the matrix inversion operator $\mathbf{R}_{\mathrm{md}}\mathbf{R}_{\mathrm{dd}}^{-1}$ can be calculated before the beginning of a measurement and then applied repeatedly. This results in calculation times that are as fast as the least-squares methods. Thus, all tested inversion algorithms are in principle able to reconstruct the temperature distributions in real-time.

4. Sensitivity studies with experimental data

For the verification of the numerical reconstruction results of all tested inversion techniques, measurements in a laboratory were performed. Such sensitivity tests with experimental data allow a tentative comparison of the inversion algorithms for their application to real atmospheric conditions.

Some years ago, a tomographic model has been designed at the Leipzig Institute for Meteorology for experimental testing of tomographic algorithms and educational purposes [34]. This model consists of a frame construction of aluminum profiles with a dimension of (1.23×1.23) m^2. Several sources and receivers may be arranged flexibly at this construction. In analogy to the numerical sensitivity tests, 8 source-receiver pairs were arranged around the area of investigation in the experiment. A detailed description of the hardware including the characteristics of the acoustic signals used in the presented

study are described in [17]. For tomographic reconstruction using least-squares methods the investigation area was subdivided into grid cells with a size of (0.3 × 0.3) m^2. This partition yields an acceptable conditioning of the sound ray segment matrix (condition number $\alpha = 9.14$) which is in good agreement with the value of the realized numerical sensitivity studies using the same number of acoustic devices. The spatial distribution of source-receiver pairs, sound rays, and grid cells is shown in Figure 4. Furthermore, the setup includes a circular heating plate positioned 0.37 m below grid cell 14. The heating plate was used to simulate heterogeneous surface conditions such that similar to the numerical sensitivity studies a temperature inhomogeneity could be generated within the tomographic array.

Due to the relatively short sound ray paths in the investigation area, inaccurate measurements of source and receiver positions as well as travel times are known to result in high uncertainties of the reconstructions [35]. Therefore, relative changes of temperature to a well known reference state were studied. The reference measurement was realized before the actual experiment assuming no flow in the laboratory. Using an Assmann psychrometer, a constant background acoustic virtual temperature of 23.3 °C was estimated. Correction factors for the acoustically determined travel times could be calculated from the differences between the acoustically measured travel times and the travel times which are calculated from the Assmann psychrometer data. These corrections were applied to all measurements during the experiment. In doing so, errors due to uncertainties from measurements of source and receiver positions can be rectified.

The experiment was organized as follows. First, travel-time measurements were conducted for a constant and homogeneous temperature distribution and no air flow in the laboratory. After 53 min the heating plate was switched on in order to generate a temperature inhomogeneity within the tomographic investigation area. After another hour (63 min) the heating plate was switched off and the temporal cooling process was observed. During the whole experiment, the repetition rate for a single tomographic measurement was chosen to be 20 s.

For the reconstructions, all tested algorithms calculated the unknown temperature fields from the measured travel-time data with the optimal parameters achieved by the previous numerical sensitivity studies. Thus, the iteration cycle of ART and MART was terminated after 10 iterations and using SIRT after 50 iterations. Furthermore, for all IRTs the same averaging processes as in the numerical studies were implemented after each iteration (see section 3). The turbulence parameters used for SI reconstructions were $l_T = 1.0$ m and $\sigma_T^2 = 0.76$ K^2.

The temperature tomograms for a representative time step, when the heating plate was switched on, are presented in Figure 5. At first view, all inversion algorithms clearly reconstructed the higher temperatures above the heating plate. However, the individual reconstructions differ in the magnitude of the maximum temperature value.

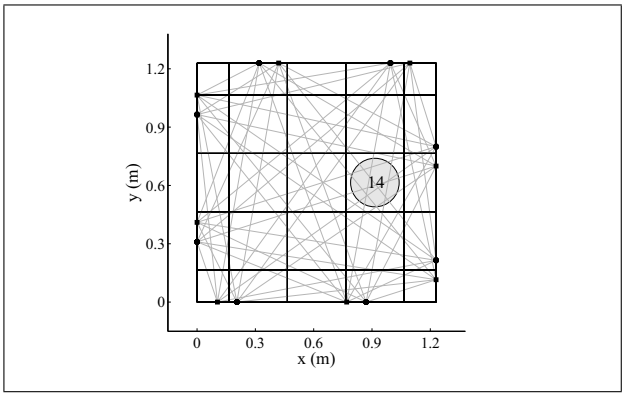


Figure 4. Setup for the experimental study. Gray lines denote sound rays between the 8 source-receiver pairs (squares and circles, respectively) passing the grid cells (black lines) with an extension of (0.3 × 0.3) m^2. The location of the heating plate within grid cell 14 (0.37 m below the tomographic array) is marked with a gray circle.

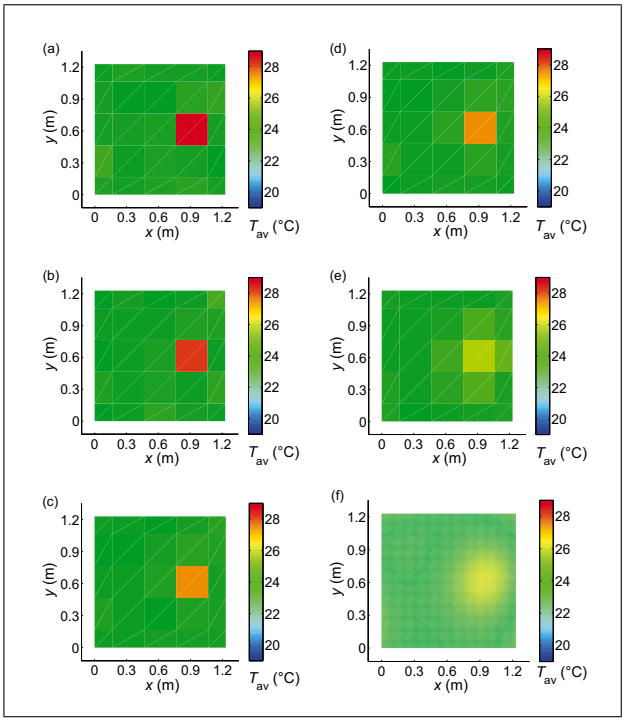


Figure 5. Tomographically reconstructed acoustic virtual temperature fields using MI (a), ART (b), MART (c), SIRT (d) and SI (e) for the setup given in Figure 4, 61 min after switching the heating plate on. The SI reconstruction with a higher spatial resolution of (0.01 × 0.01) m^2 is shown in (f).

The differences between the results of the five algorithms are comparable to the results of the numerical sensitivity studies. Moreover, this holds for the whole experiment which is graphically illustrated in Figure 6. It shows the temporal development of the temperature value within grid cell 14, which was directly influenced by the heating plate.

At the beginning of the experiment, all algorithms estimated nearly the same temperature values. Approximately 80 s after switching the heater on, all inversion algorithms reconstructed a warming in the observed grid cell. Af-

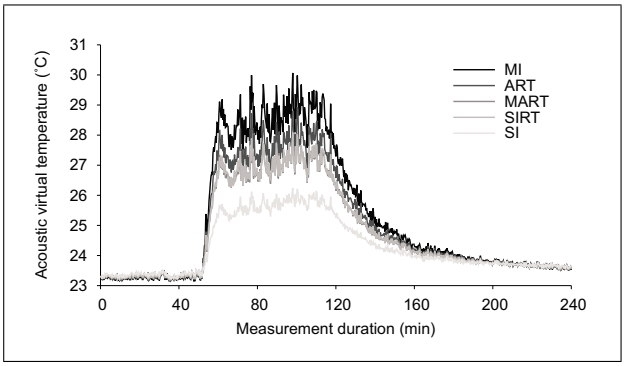


Figure 6. Temporal evolution of the acoustic virtual temperature within grid cell 14 in a laboratory experiment. The temperature values are reconstructed using MI, ART, MART, SIRT, and SI. At the beginning, the measurements were performed during stable conditions in the laboratory. After 53 min a heating plate below cell 14 was switched on for one hour (63 min) to generate a temperature inhomogeneity.

ter another 10 min this rise in temperature slowed down and finally stopped. Subsequently, temperature fluctuations were observed, which partly exceeded 1.0 K, and are qualitatively comparable between all inversion techniques. On the one hand, this process was caused by aperiodic heating of the heating coil. On the other hand, it may be produced by a generation of warm air bubbles which do not rise continuously from the heated surface. Thus, random thermal eddies may contribute to the fluctuations of the temperature value within cell 14.

As it can be seen in Figure 6 the temperature values reconstructed by SIRT and MART are nearly identical which is in good agreement with the numerical results. Also the results of MI and ART are similar to the numerical ones. MI determined the highest warming which is conform to the overestimation of the maximum temperature in the numerical studies whereas the results of ART are to be found between the results of MI and SIRT (MART). The estimated temperature values of SI are smaller than the ones of the other algorithms, which seems not be in agreement with the former numerical studies. However, upon reconsideration of the results in Figure 3b, there can be cases with a high temperature difference within the tomographic array, where the RMSE value of SI exceeds the value of SIRT. These specific results of the numerical studies were achieved for nearly ideal conditions. However, during the laboratory experiment the determined travel-time data are corrupted with noise which influenced the conditioning of the data-data covariance matrix calculated using SI. Without regularization, the $\mathbf{R_{dd}}$ matrix for the experimental setup was ill-conditioned such that the SI results were too noisy, thus not allowing a meaningful data analysis. For this reason, extensive parameter studies are performed to obtain reasonable solutions for the current setup. The best results were achieved for the above mentioned turbulence parameters and after regularization of $\mathbf{R_{dd}}$ considering a travel-time error of 200 ns in the data. Using this noise term, the structure of the heating plate became visible in the tomograms and the significant artifacts were suppressed. In contrast, the solution was smoothed very strong such that the temperature value in grid cell 14 reconstructed by SI is much smaller than the values reconstructed by least-squares methods. According to the numerical studies, an increased travel-time error produced even smoother fields (nearly homogeneous temperature fields) whereas a decreased travel-time error produced artifacts. Based on these results the used turbulence model appears to be not suitable to reconstruct such relatively high temperature differences along distances of a few decimeters. There is evidence that in such cases the applied SI algorithm is not as robust as IRTs.

For the least-squares methods the travel-time errors can not simply be separated and caused no positive effect with respect to the solution as for SI. Hence, noise is not explicitly taken into consideration during data evaluation. As an estimation a travel-time error of 200 ns along a sound ray path with a distance of 1.29 m results in a temperature error of 0.03 K along this path.

Furthermore, Figure 6 shows that after switching the heating plate off, the differences between the temperatures reconstructed by the tested algorithms decrease with decreasing magnitude of the temperature inhomogeneity. This is again conform with the results of the numerical study, that small temperature differences within the investigated area can be better reconstructed compared to extreme structures.

To assess the temperature differences between the reconstructions of the individual inversion algorithms, the reconstruction errors have to be estimated. In a real experiment the reconstruction error is composed of the measurement error, the discretization error, and the inversion error [7]. The measurement error includes the error of the travel-time determination and the uncertainty of the position of acoustic devices. The latter was eliminated in this studies because changes of the temperature field were measured relatively to a known initial distribution. The discretization error arises of the fact that a continuous temperature distribution can not be exactly approximated by the discretized field as well as that the forward modeling of the travel-time data from the discretized temperature field is different compared to the measured data from the continuous field [7]. The inversion error consists of the errors which result from the individual algorithms. Using least-squares methods, ill-posed inversion problems typically yield solutions such that additional information is required to chose a suitable solution which is also necessary for stochastic methods.

An analysis of the uncertainty in temperature reconstruction using least-squares methods was performed by calculating the covariance about the true solution $\sigma_\tau^2(\mathbf{L}^T\mathbf{L})^{-1}$ [2]. As a result of this calculation an uncertainty of the temperature value within grid cell 14 of 0.6 K was estimated for one single measurement. This uncertainty is predictable assuming no correlation between the noise in the system of equations and a constant variance of the measured travel times. With regard to the temper-

ature values during constant conditions as well as during the cooling process (cp. Figure 5), absolute differences between the reconstructions of the different algorithms are in the range of the theoretically estimated uncertainty. Thus, in these cases all least-squares algorithms produce comparable reconstruction results.

In contrast to the least-squares methods, SI has the advantage to visualize small-scale turbulent structures within the tomographically observed medium due to the possibility to calculate temperature distributions of highly spatial resolution. In Figure 5f a temperature tomogram reconstructed by SI using a spatial resolution of (0.01×0.01) m^2 is presented for the same data as in Figure 5e. The location of the heating plate is well reproduced with a high spatial resolution in the temperature distribution. Consequently, SI algorithms are favored for atmospheric applications which aim at analyzing small-scale turbulence. According to the results in [11], atmospheric turbulent structures can be well reconstructed using a Gaussian covariance function and a suitable correlation length. However, the variance of temperature fluctuations still needs to be determined with a conventional measuring instrument positioned near the investigation area. From this measurements it can be deduced whether measured travel-time variations are caused by a change of atmospheric conditions or by measurement noise.

5. Conclusions

The study was designed to primarily assess the reconstruction accuracy of five different inversion techniques used in acoustic travel-time tomography of the atmosphere. The focus was set on reconstructions of two-dimensional temperature distributions. Therefore, synthetically generated as well as experimental travel-time data were used as input for the inversion algorithms.

The analysis of numerical travel-time data showed that the algorithms MI and ART produce greater temperature errors compared to SIRT, MART, and SI, especially at the location of the temperature inhomogeneity and near the border of the tomographic array. A common property of all algorithms is the fact that with increasing temperature contrasts within the area of investigation the RMSE values of the reconstructed fields increase as well. Nevertheless, the results of this study show that the algorithms SIRT, MART, and SI are favorable to characterize a natural temperature field regarding its degree of heterogeneity. The purpose of the underlying investigation plays a key role in choosing a suitable algorithm. For instance, to monitor a temperature field within a certain area SIRT as well as MART are preferable for engineering applications because the algorithms are very robust concerning high temperature differences in the investigation area. Furthermore, they allow a fast real-time interpretation of the measured data without additional explicit information. An adverse property of least-squares methods is the dependency on the conditioning of the sound ray segment matrix such that the spatial resolution of the temperature distributions is limited using these techniques. In contrast, SI is able to reconstruct spatially highly resolved and accurate temperature fields when the choice of the turbulence parameters is adequate. Therefore, SI is favored for applications which aim at analyzing and visualizing small-scale structures like atmospheric turbulence. Moreover, high memory capacities and the knowledge about the turbulence parameters and measurement errors for SI potentially allow both SI and least-squares methods being used to perform real-time analysis of measured data.

A special characteristic of acoustic travel-time tomography to estimate spatial distributions of temperature or flow is that the method itself is scalable and can be used in the laboratory as well as for outdoor investigations where sound ray path lengths may extend up to several hundred meters. Thus, results which are obtained in this study are also valid for tomographic arrays of larger dimensions. Only parameter settings, like grid cell size or the turbulence parameters, have to be adapted. Furthermore, the algorithms and the results of this study are not only limited to acoustic travel-time tomography of the atmosphere but can also be used in other scientific areas, e.g., for DOAS tomography [7] or GNSS water vapor tomography [9].

Further work should focus on comparing the behavior of the different algorithms in field studies in the atmospheric boundary layer. Therefore, the additional influence of the wind vector on the sound propagation has to be considered. Furthermore, a detailed study of the characteristics of the inversion techniques for simultaneous reconstructions of two-dimensional or three-dimensional temperature and wind speed distributions within a tomographic array still remains.

Acknowledgments

We would like to thank S. Vecherin for his help to implement the stochastic inversion for our study as well as A. Raabe for the fruitful discussions of the results.

References

[1] N. Rawlinson, S. Pozgay, S. Fishwick: Seismic tomography: A window into deep earth. Physics of the Earth and Planetary Interiors **178** (2010) 101–135.

[2] W. Munk, P. Worcester, C. Wunsch: Ocean acoustic tomography: A scheme for large scale monitoring. Cambridge University Press, New York, 1995, 433 S.

[3] D. K. Wilson, D. W. Thomson: Acoustic tomographic monitoring of the atmospheric surface-layer. J. Atmos. Ocean. Technol. **11** (1994) 751–769.

[4] A. Ziemann, K. Arnold, A. Raabe: Acoustic tomography as a method to identify small-scale land surface characteristics. Acta Acustica **87** (2001) 731–737.

[5] S. N. Vecherin, V. E. Ostashev, D. K. Wilson: Three-dimensional acoustic travel-time tomography of the atmosphere. Acta Acustica united with Acustica **94** (2008) 349–358.

[6] V. E. Kunitsyn, E. D. Tershchenko: Ionospheric tomography. Springer-Verlag Berlin Heidelberg New York, 2003, 259 S.

[7] T. Laepple, V. Knab, K. U. Mettendorf, I. Pundt: Longpath DOAS tomography on a motorway exhaust gas plume: numerical studies and application to data from the BAB II campaign. Atmos. Chem. Phys. **4** (2004) 1323–1342.

[8] I. Pundt, K.-U. Mettendorf, T. Laepple, V. Knab, P. Xie, J. Lösch, C. Friedeburg, U. Platt, T. Wagner: Measurements of trace gas distributions using Long-path DOAS-Tomography during the motorway campaign BAB II: experimental setup and results for NO2. Atmospheric Environment **39** (2005) 967–975.

[9] M. Bender, R. Stosius, F. Zus, G. Dick, J. Wickert, A. Raabe: GNSS water vapour tomography - Expected improvements by combining GPS, GLONASS and Galileo observations. Advances in Space Research **47** (2011) 886–897.

[10] J. Radon: Über die Bestimmung von Funktionen durch ihre Integralwerte längs gewisser Mannigfaltigkeiten. Ber. Sächs. Akad. Wiss. **69** (1917) 262–277.

[11] V. E. Ostashev, S. N. Vecherin, D. K. Wilson, A. Ziemann, G. H. Goedecke: Recent progress in acoustic travel-time tomography of the atmospheric surface layer. Meteorol. Z. **18** (2009) 125–133.

[12] J. L. Spiesberger, K. M. Fristrup: Passive localization of calling animals and sensing of their acoustic environment using acoustic tomography. Am. Natural. **135** (1990) 107–153.

[13] D. K. Wilson, V. E. Ostashev, S. N. Vecherin, A. G. Voronovich, S. L. Collier, J. M. Noble: Assessment of acoustic travel-time tomography of the atmospheric surface layer. Proceedings of AMS Symposium on Boundary Layers and Turbulence, Portland, ME, 2004.

[14] S. N. Vecherin, V. E. Ostashev, G. H. Goedecke, D. K. Wilson, A. G. Voronovich: Time-dependent stochastic inversion in acoustic travel-time tomography of the atmosphere. J. Acoust. Soc. Am. **119** (2006) 2579–2588.

[15] A. Ziemann, K. Arnold, A. Raabe: Acoustic tomography in the atmospheric surface layer. Ann. Geophysicae **17** (1999) 139–148.

[16] K. Arnold, A. Ziemann, A. Raabe, G. Spindler: Acoustic tomography and conventional meteorological measurements over heterogeneous surfaces. Meteorol. Atmos. Phys. **85** (2004) 175–186.

[17] M. Barth, A. Raabe, K. Arnold, C. Resagk, R. Du Puits: Flow field detection using acoustic travel time tomography. Meteorol. Z. **16** (2007) 443–450.

[18] W. Menke: Geophysical data analysis: Discrete inverse theory. International Geophysical Series, Volume 45, Academic Press, London, 1989, 289 S.

[19] V. E. Ostashev: Acoustics in Moving Inhomogeneous Media. E & FN Spon, 1997.

[20] D. C. Miller: Sound waves - their shape and speed. The Macmillian Company, New York, 1937, 164.

[21] M. Barth, A. Raabe: Acoustic tomographic imaging of temperature and flow fields in air. Measurement Science & Technology **22** (2011) 035102.

[22] E. Anderson, Z. Bai, C. Bischof, S. Blackford, J. Demmel, J. Dongarra, J. Du Croz, A. Greenbaum, S. Hammarling, M. A., D. Sorensen: Lapack user's guide. SIAM, Philadelphia, 1999.

[23] T.-W. Lo, P. L. Inderwiesen: Fundamentals of seismic tomography. Geophysical Monograph Series 6, Society of Exploration Geophysicists, 1994, 178 S.

[24] S. Petra, C. Popa, C. Schnörr: Accelerating Constrained SIRT with Applications in Tomographic Particle Image Reconstruction. Tech. Rept. IWR, University of Heidelberg, 2009.

[25] F. Natterer: The Mathematics of Computerized Tomography. Teubner-Wiley, Reprinted in SIAM Classics in Applied Mathematics, 1986.

[26] R. Gordon, R. Bender, G. T. Herman: Algebraic reconstruction techniques (ART) for three-dimensional electron microscopy and x-ray photography. J. Theor. Biol. **29** (1970) 471–481.

[27] P. Gilbert: Iterative methods for the three-dimensional reconstruction of an object from projections. J. Theor. Biol. **36** (1972) 105–117.

[28] R. B. Stull: An Introduction to Boundary Layer Meteorology. Kluwer Academic Publisher, 1988, 666.

[29] D. K. Wilson, A. Ziemann, V. E. Ostashev, A. G. Voronovich: An overview of acoustic travel-time tomography in the atmosphere and its potential applications. Acta Acustica **87** (2001) 721–730.

[30] S. N. Vecherin, V. E. Ostashev, D. Wilson, A. Voronovich, G. Goedecke, S. Collier, J. Noble, D. Ligon: Forward and inverse problems of acoustic tomography of the atmosphere. Proc. 11th Intern. Symp. on Long Range Sound Propagation, Fairlee, VT (2004).

[31] L. N. Trefethen, D. Bau: Numerical linear algebra. SIAM, 1997, 361.

[32] M. Barth, A. Raabe: Akustische Tomographie zur gleichzeitigen Bestimmung von Temperatur- und Strömungsfeldern in Innenräumen. Wiss. Mitt. Inst. für Meteorol. Univ. Leipzig **37** (2006) 71–80.

[33] K. Niachou, I. Livada, M. Santamouris: Experimental study of temperature and airflow distribution inside an urban street canyon during hot summer weather conditions–part I: Air and surface temperatures. Building and Environment **43** (2008) 1383–1392.

[34] P. Holstein, A. Raabe, R. Müller, M. Barth, D. Mackenzie, E. Starke: Acoustic tomography on the basis of traveltime measurement. Measurement Science & Technology **15** (2004) 1420–1428.

[35] M. Barth: Akustische Tomographie zur zeitgleichen Erfassung von Temperatur- und Strömungsfeldern. Wiss. Mitt. Inst. Meteorol. Univ. Leipzig **44** (2009) 178.